



Experimental and numerical investigation on the crashworthiness optimization of thin-walled aluminum tubes considering damage criteria

Sinem K. Mert¹ · Murat Demiral^{2,3} · Murat Altin⁴ · Erdem Acar⁵ · Mehmet A. Güler^{2,5} 

Received: 1 October 2020 / Accepted: 22 December 2020 / Published online: 3 February 2021
© The Brazilian Society of Mechanical Sciences and Engineering 2021

Abstract

This paper aims to investigate the crashworthiness performance of thin-walled tubes under quasi-static conditions both experimentally and numerically. Single-cell and multi-cell tubes made of aluminum were tested under quasi-static compressive loading. A three-dimensional finite element (FE) model accounting for the damage in the constitutive equations was developed. It was validated through experiments based on the force–displacement behavior and the deformation views of the tubes. The sensitivity of the initial peak force, total energy absorption, specific energy absorption, and crush force efficiency to different model parameters such as the tube height and thickness, velocity of the rigid upper plate, and the type of the constitutive equations used were investigated in detail. It was observed that the element type used (shell/solid) in the FE model and the element size in the thickness direction played an important role in simulating the tests accurately. In addition, surrogate-based optimization of the single-cell tubes (T0) and two different types of multi-cell tubes (T4E, T8E) is performed to maximize crush force efficiency (CFE) and specific energy absorption (SEA). It is found that CFE of the optimum T4E design is 8.5% greater than CFE of the optimum T8E design and 30% greater than CFE of the optimum T0 design. It is also found that SEA of the optimum T4E design is 9.8% greater than SEA of the optimum T8E design and 213% greater than SEA of the optimum T0 design.

Keywords Thin-walled aluminum tubes · Crashworthiness · Specific energy absorption · Quasi-static crushing · Damage criteria · Surrogate-based optimization

1 Introduction

Various safety systems are used in the automotive industry to ensure the safety of drivers and passengers in the event of an accident. Passive safety systems such as seat belts, airbags, thin-walled tubes are installed in vehicles to reduce

the severity of a crash. Thin-walled structures, which are the commonly used elements, usually have a tubular structure and are capable of absorbing the energy generated due to inelastic deformation during collision. In recent decades, tubular structures made of aluminum have been studied for this purpose due to their superior energy absorption performance and low cost.

Technical Editor: João Marciano Laredo dos Reis.

✉ Mehmet A. Güler
mehmet.guler@aum.edu.kw; maguler@alum.lehigh.edu

Sinem K. Mert
sinemkocaoglanmert@gmail.com

Murat Demiral
murat.demiral@aum.edu.kw

Murat Altin
maltin@gazi.edu.tr

Erdem Acar
acar@etu.edu.tr

¹ Department of Mechanical Engineering, Ankara Yildirim Beyazit University, Ankara 06010, Turkey

² College of Engineering and Technology, American University of the Middle East, Egaila 54200, Kuwait

³ Department of Mechanical Engineering, University of Turkish Aeronautical Association, Ankara, Turkey

⁴ Department of Automotive Engineering, Gazi University, Ankara, Turkey

⁵ Department of Mechanical Engineering, TOBB University of Economics and Technology, Ankara 06560, Turkey

Quite a few studies are available in the literature investigating the crashworthiness performance of tubes experimentally and/or numerically [1–10]. Fu et al. [1] studied the crush performance of four-layer tubes (304 stainless steel) with U-shaped corrugations. They compared the experimental and theoretical energy absorption data of impacted tubes of different drop heights. Demirci and Yildiz [2] investigated the effect of conventional steel, new generation DP-TRIP steels, AA7108–AA7003 aluminum alloys, AM60 – AZ31 magnesium alloys on crashworthiness of thin-walled tubes numerically. They found that the energy absorption capability of steel tubes was better than aluminum and magnesium tubes. However, specific energy absorption capacity of tubes made from lightweight materials is higher the steel tubes. According to their results, the polygonal and circular tubes performed better performance than square and rectangular tubes for all materials in terms of total energy absorption and the specific energy absorption. Paygozar et al. [3] investigated a system consists of expanded circular tube with two inner tubes to enhance energy absorption. Demirci and Yildiz [4] developed a new tube design and showed the significance of the tube geometry, the number and position of the spot welds and sheet-metal thickness on crash performance. Various tube designs were created by changing the geometrical parameters of the thin-walled structures to enhance the energy absorption performance of the structures. Guler et al. [5] studied the effect of geometrical parameters on crashworthiness of tubes under axial impact loading. Circular tubes had better performance in terms of crush force efficiency, and the peak forces were lowered with corrugations. Rouzegar et al. [6] investigated perforated metal and composite-metal tubes loaded axially. The effects of number and diameter of holes on crashworthiness parameters in terms of peak force, specific absorbed energy and crush force efficiency were studied. Hu et al. [7] investigated the energy absorption characteristics of the foam-filled tri-tube under quasi-static crushing conditions. They compared the energy absorption characteristics of empty and foam-filled versions of single, double and tri-tubes and found that foam-filled tri-tubes showed the best performance. Attar et al. [8] studied the effect of the multi-cell columns combined with stiffeners to the outer tube wall for enhancing the energy absorption. The effect of the number and arrangement of stiffeners in the multi-cell structures was investigated in this study. They observed that adding stiffeners in the outer wall increased the SEA and the use of multi-cell columns increased the CFE. Baykasoglu and Cetin [9] investigated the effects of thickness-gradient patterns on crash performances of thin-walled circular tubes under impact loading by using the explicit FE method. They reduced the maximum crush force and increased the SEA and CFE values by selecting appropriate thickness-gradient patterns. Altin et al. [11] evaluated the effect of foam

filling on the crashworthiness performance of multi-cell square and circular tubes. They found that SEA of foam-filled square tube was 5 times higher than the empty square tube with minimum SEA. The SEA and CFE performances of the foam-filled square tube were increased by 87% and 42% by changing the wall thickness, respectively. Similarly, Altin et al. [12] optimized the energy absorption capacity of aluminum foam-filled multi-tubular circular structures. They found that lateral foam-filled tubes had 19% higher CFE and 6% higher SEA than axial foam-filled tubes. Also, tri-tubular structures with a large thickness and a taper angle had maximum CFE and SEA. Sarkabiri et al. [10] optimized the crashworthiness parameters of thin-walled grooved conical tubes made of 6061-T6 aluminum alloy. They simulated tubes filled with polyurethane foam with grooves on the internal and external surfaces under quasi-static loading condition. The density of polyurethane foam and geometric parameters of the tube were optimized through multi-objective optimization process. Their numerical results showed the importance of grooves depth and thickness of the tube. Researchers also focused on optimization algorithms. The performances of the optimization algorithms were investigated quantitatively and qualitatively in the study of Yildiz et al. [13].

Thin-walled circular structures collapse symmetrically or non-symmetrically due to the ratio of the diameter to thickness of the structure [14]. However, most of the square tubes do not undergo progressive collapse; instead, they go through splitting or unexpected collapse modes. The literature mentioned briefly in the previous paragraph was related to the crashworthiness studies of aluminum tubular structures in which the failure was not accounted for. There are few numerical studies in the literature about the crashworthiness of thin-walled structures under compression that also accounts for the failure in the finite element analysis (FEA) model. Kim et al. [15] tested and simulated aluminum AA7003-T7 tubes with various cross sections including rectangular, octagonal, and hexagonal. A severe deformation in the middle region of the specimen with folding was reported. Octagonal tubes showed better energy absorption performance and higher mean load than the others. Reyes et al. [16] tested square tubes made of aluminum (AA6060) under oblique loading. Thickness and heat treatment effects on the energy absorbing capability were analyzed. Qiao et al. [17] performed a crashworthiness study of aluminum tubes with different thicknesses, section dimensions, and impact velocities. Geometric imperfections and a damage model were introduced to square tubes in order to validate the developed model. Marzbanrad et al. [18] investigated the crushing of a circular tube made of aluminum 7108-T6. In the model, the boundary conditions and the ductile failure criterion were analyzed. The results showed that applying an elastic boundary condition could change the deformation mode and increase the peak force. In the studies

of Allahbakhsh et al. [19] and Estrada et al. [20, 21], different numerical models were developed for EN AW-7108 T6 based on the damage model of Hooputra et al. [22]. In these studies, as damage initiation criteria shear, ductile, and MSFLD models were used. Estrada et al. [20, 21] studied the impact of geometry on the energy absorption performance of multi-cell structures and the impact of circular hole discontinuities on the energy absorption performance of tubes, respectively. Applying circular hole discontinuities decreased the peak force by up to 4.74% with respect to a tube without discontinuities. In the other study of Estrada et al. [23], the progressive damage modeling of aluminum 6063-T5 bi-tubular structures with various cross sections including circular discontinuities was investigated. They were modeled using Johnson–Cook (J–C) damage model. A buckling effect was observed when the hole was at the mid-section.

Crashworthiness of aluminum tubes under quasi-static conditions was investigated extensively in the literature. Usually, two-dimensional shell elements are used in both industry (automotive, aerospace and related industries) and academia including the above-mentioned references to model thin-walled tubular structures. The main assumption when using shell elements is to ignore the third (out-of plane) component of the stress field [24]. However, these shell models sometimes cannot capture the physical deformation shape as was the case in the initial works of this study. Similarly, Jirawattanakasem and Bureerat [25] showed that the contact force is better captured using solid elements rather than the shell elements in their FEA simulations of tolerance ring assembly installation process. Therefore, a systematic investigation is needed on this issue, and according to the best of our knowledge, there is not many research in the open literature. To fill this gap, both experimental and numerical studies are performed in order to understand the results of the parameters used in the FE model on the crashworthiness performance and deformation shapes of single cell and multi-cell tubes. The investigated parameters include tube height, wall thickness, velocity of the rigid upper plate, and the type of finite elements used in discretization of the tubes. Moreover, two different novel multi-cell tubes are designed. Their crashworthiness performances are compared and contrasted with respect to the baseline (single cell) design experimentally and numerically.

This work is organized as follows: In the following part, the definitions of different metrics used to describe crashworthiness are provided. In Sect. 3, details about the performed experiments are given. In Sect. 4, the developed numerical model incorporating the material model is presented. In Sect. 5, comparisons with experiments and sensitivity analysis for various parameters are provided. In Sect. 6, details of surrogate-based optimization of the single-cell and multi-cell tubes are discussed. Finally, in Sect. 7, concluding remarks that can be drawn from this study are outlined.

2 Crashworthiness criteria

Usually, total energy absorption (E_{absorbed}), specific energy absorption (SEA), mean crushing force (MCF), initial peak force (IPF), and crush force efficiency (CFE) are most commonly used metrics to measure the crashworthiness performance of thin-walled tubes.

The force–displacement curve of the impact is integrated to determine the total energy absorption (E_{absorbed}) and formulated as:

$$E_{\text{absorbed}} = \int_0^{x_d} F dx \quad (1)$$

The mean crushing force (MCF) is the constant force that would give the same absorbed energy until the end of deformation (x_d) and may be expressed as:

$$\text{MCF} = \frac{E_{\text{absorbed}}}{x_d} \quad (2)$$

The crush force efficiency (CFE) is calculated using the following equation:

$$\text{CFE} = \frac{\text{MCF}}{\text{IPF}} \quad (3)$$

Initial peak force which is a significant indicator can be defined as the initial maximum crush load. Total energy absorption (E_{absorbed}) is divided by the tube mass (m) to obtain specific energy absorption (SEA):

$$\text{SEA} = \frac{E_{\text{absorbed}}}{m} \quad (4)$$

In the foregoing analysis, the values of E_{absorbed} , SEA and CFE were calculated and tabulated in order to compare the results obtained from simulations and experiments.

3 Experimental setup

In this section, the experimental setup used to determine the crashworthiness of hollow single-cell and multi-cell tubes under axial loading is explained.

3.1 Details of the quasi-static tests

The test specimens were made of Al 6061-T6. The cross section of each single-cell tube was 71.5 mm × 86.5 mm, height was 180 mm, and wall thickness was 1.5 mm (as shown in Fig. 1). Similarly, multi-cell tubes with two different geometry, labeled as T4E and T8E based on the number of rectangular space in the cross section, were produced

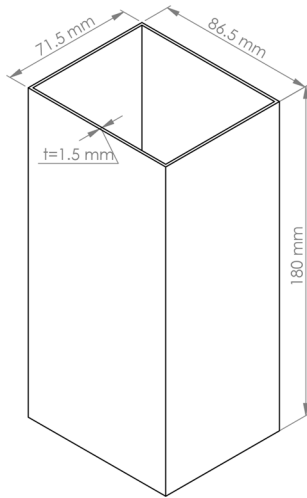


Fig. 1 Geometric details of the single-cell tube: t denotes thickness of the tube

with the same height and wall thickness as shown in Fig. 2. Novel design for multi-cell tubes was obtained as follows.

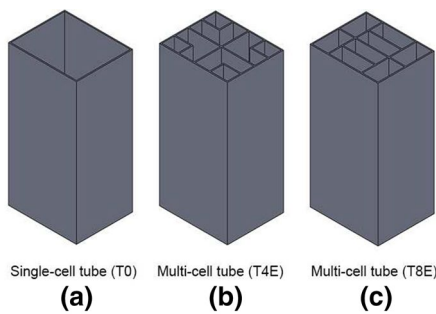


Fig. 2 Geometric views and manufactured test specimens for different tube configurations **a** single-cell (T0) **b** multi-cell (T4E) **c** multi-cell (T8E)

Multi-cell tube T4E was obtained by subdividing single-cell tube by 4 and adding square tubes to corners. Multi-cell tube T8E was obtained by subdividing single-cell tube 2 and dividing each part to smaller tubes. Due to the need for a few number of tubes, the tubes were produced using the wire erosion method to ensure the accuracy of measurement. Al 6061-T6 is an extrudable material that allows mass production to be done at a low cost in an easy and fast manner.

The quasi-static tests of the tubes were performed using the INSTRON 600 LX with a load capacity of 600 kN. A bottom plate with a depth of 5 mm, which was compatible with the tubes, was produced by industrial type CNC milling machine to make the tubes stable between the two blocks during the tests. The tubes were fixed to the floor, and they did not shift during the press (as shown in Fig. 3a, b).

A constant velocity, 2 mm/min, was applied throughout all the experiments. When the displacement reached the level of full compaction, the specimens were unloaded and the test was stopped.

3.2 Experimental results of single-cell and multi-cell tubes

The force–displacement graph of the single-cell and multi-cell tubes subjected to quasi-static conditions is shown in Fig. 4. Repeatability of the experiments was ensured by conducting the identical tests with three different specimens with the same cross section.

Similar interrelation between the crush force and displacement of the tubes under the quasi-static conditions could be easily observed. An initial peak force was observed during the progressive folding. Although another peak force was observed at 30 mm deformation for specimen 3

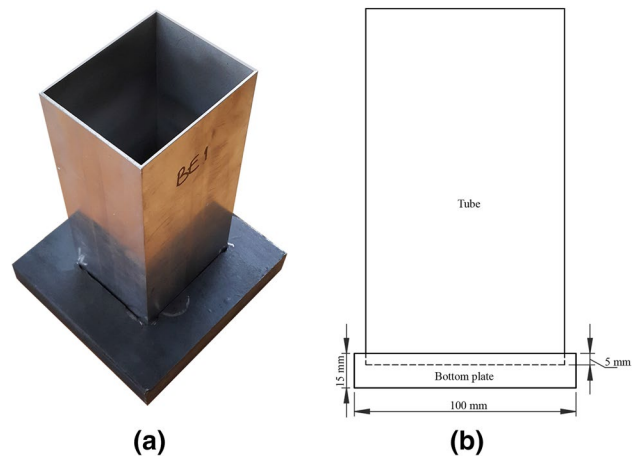


Fig. 3 Test specimen for single-cell tube with the bottom plate **a** test specimen **b** geometric details of the bottom plate. Note that, tube height is 180 mm

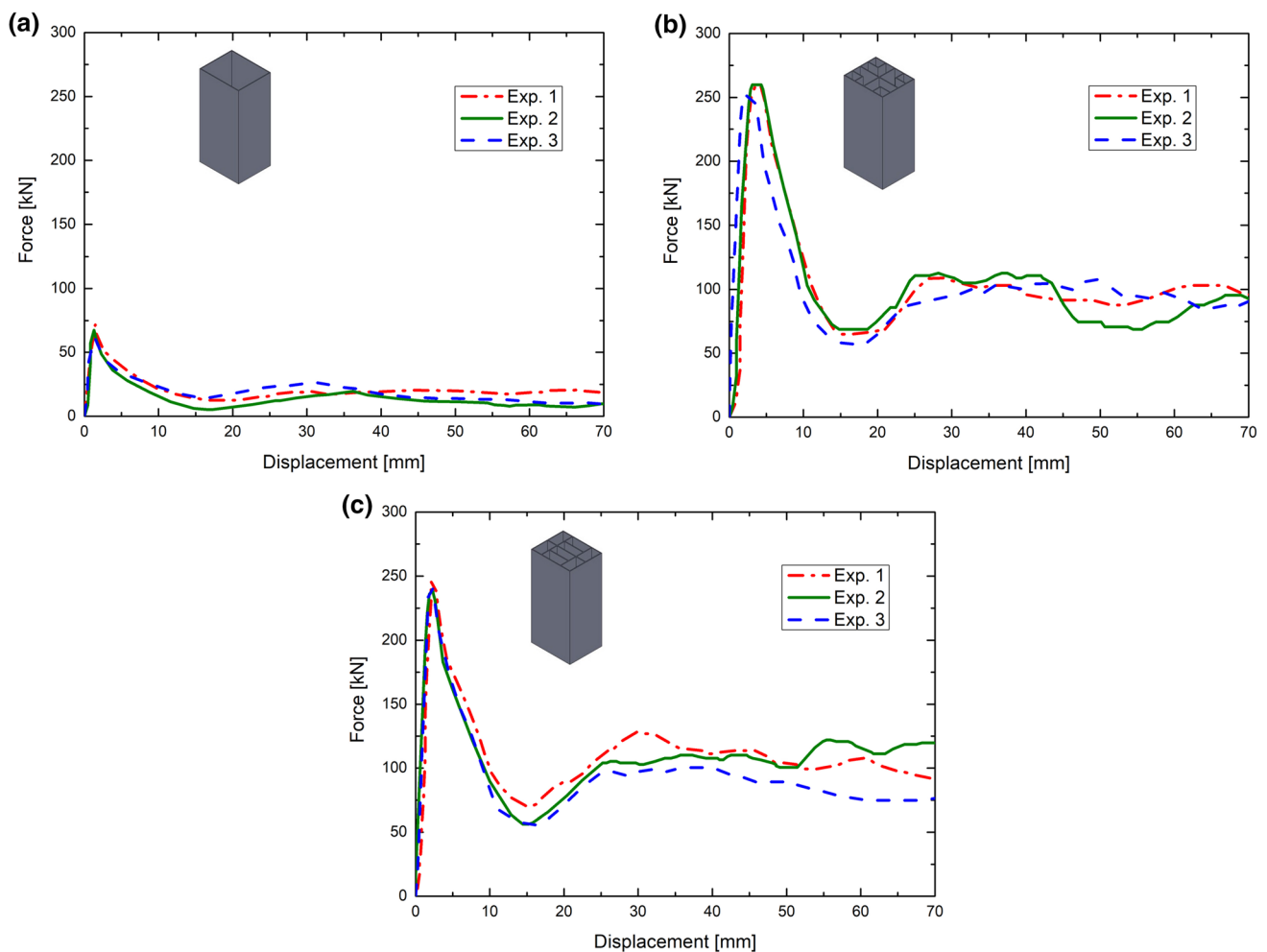


Fig. 4 Force–displacement behavior of test specimens **a** single-cell (T0) **b** multi-cell (T4E) **c** multi-cell (T8E)

of single-cell tubes, the other specimens showed a more damped behavior in Fig. 4.

The deformation process of single-cell T0 and multi-cell T4E and T8E tubes taken at certain points of displacement also had novel characteristics as shown in Figs. 5, 6 and 7. Tearing and splitting of the tube walls at the mid-height of the specimens were observed after deformation started. Similar folding shapes were observed in few studies for aluminum alloys. For example, Kim et al. [15] and Qiao et al. [17] observed folding at the mid-heights of the test specimens and modeled the deformations in their studies via LS DYNA and ABAQUS, respectively.

4 Finite element model

This section provides the details of the Fe model and detailed descriptions of the material model used in the developed FE model.

4.1 Description of the FE model

Numerical analyses were carried out using a commercial FE program ABAQUS/Explicit to model the progressive failure of the aluminum tubes. Due to nonlinearity arises from the geometry and material used, the complex contact conditions, and the local instability during crush, the implicit method has its inherent convergence difficulties; hence, it is not preferred here. It is known that, as the explicit time integration scheme requires smaller time steps depending on the smallest element size in the model, the computational time for the studied quasi-static problem is excessive. To avoid this, the automatic mass scaling technique was used to make the time increment larger. It was ensured that the ratio of the kinetic energy to the strain energy was less than 10^{-4} to properly model this quasi-static problem without introducing an artificial strength enhancement to the model.

In the model, the aluminum tube having dimensions exactly the same as the test specimen given in Fig. 3 was discretized with C3D8R hexahedron continuum solid elements

Fig. 5 Progressive failure behavior of single-cell test specimens (T0) at different stages: $d = 0$ mm, $d = 35$ mm, $d = 70$ mm **a** test specimen TOS1 **b** test specimen TOS2 **c** test specimen TOS3

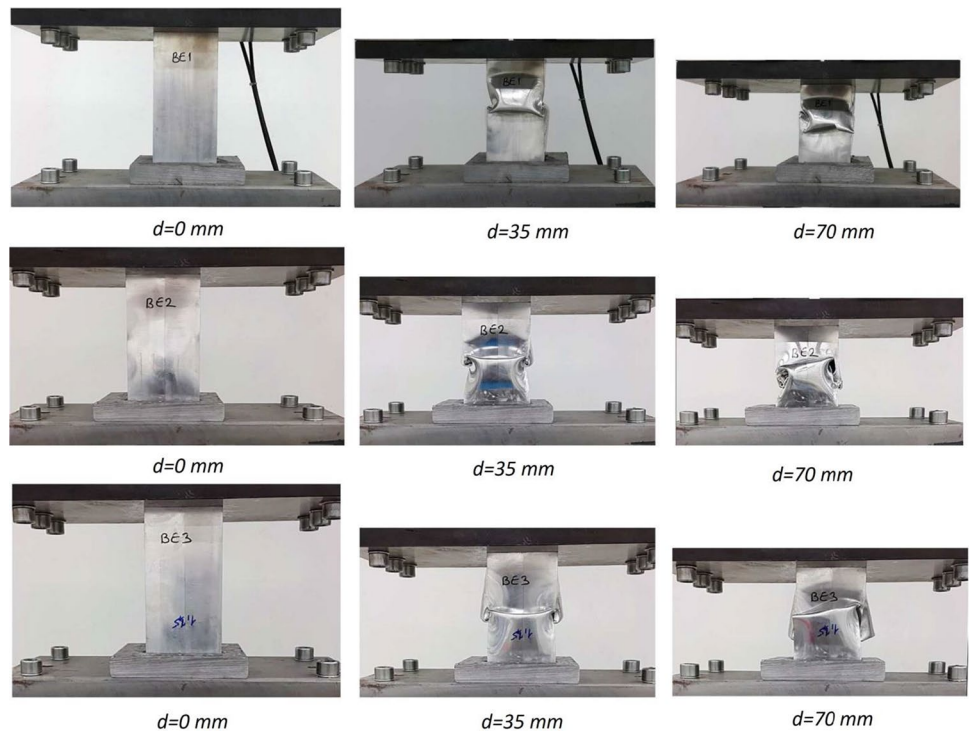


Fig. 6 Progressive failure behavior of multi-cell test specimens (T4E) at different stages: $d = 0$ mm, $d = 35$ mm, $d = 70$ mm **a** test specimen T4E1 **b** test specimen T4E2 **c** test specimen T4E3

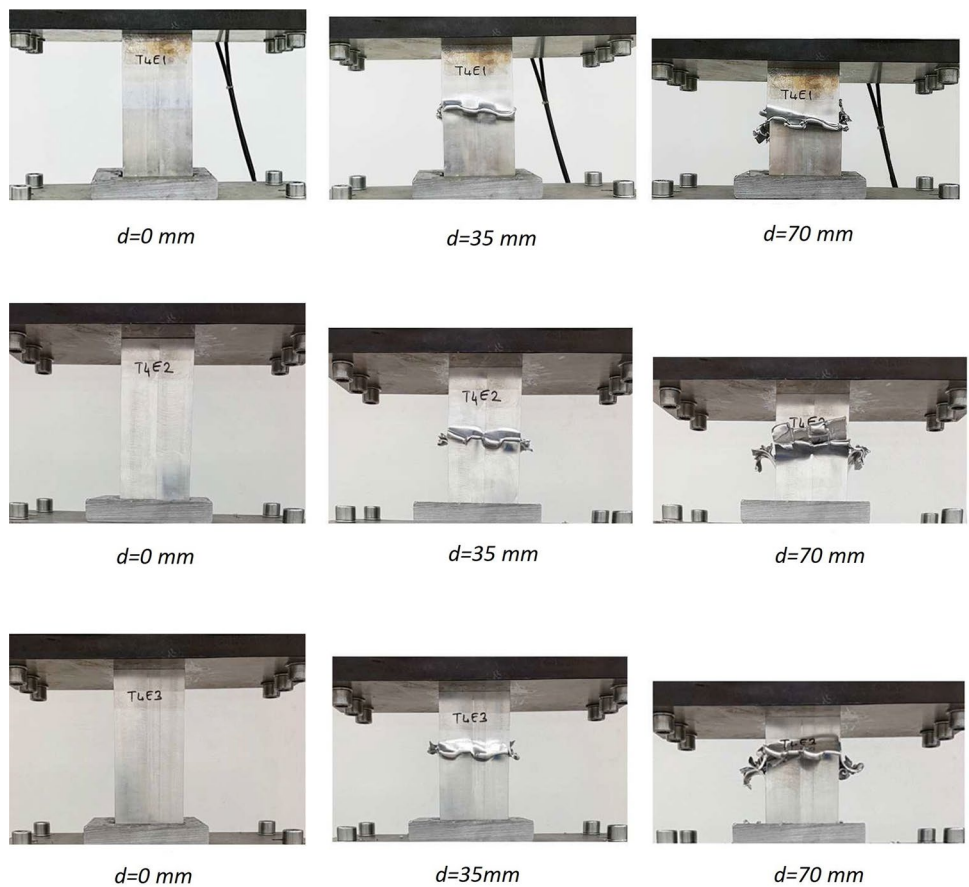
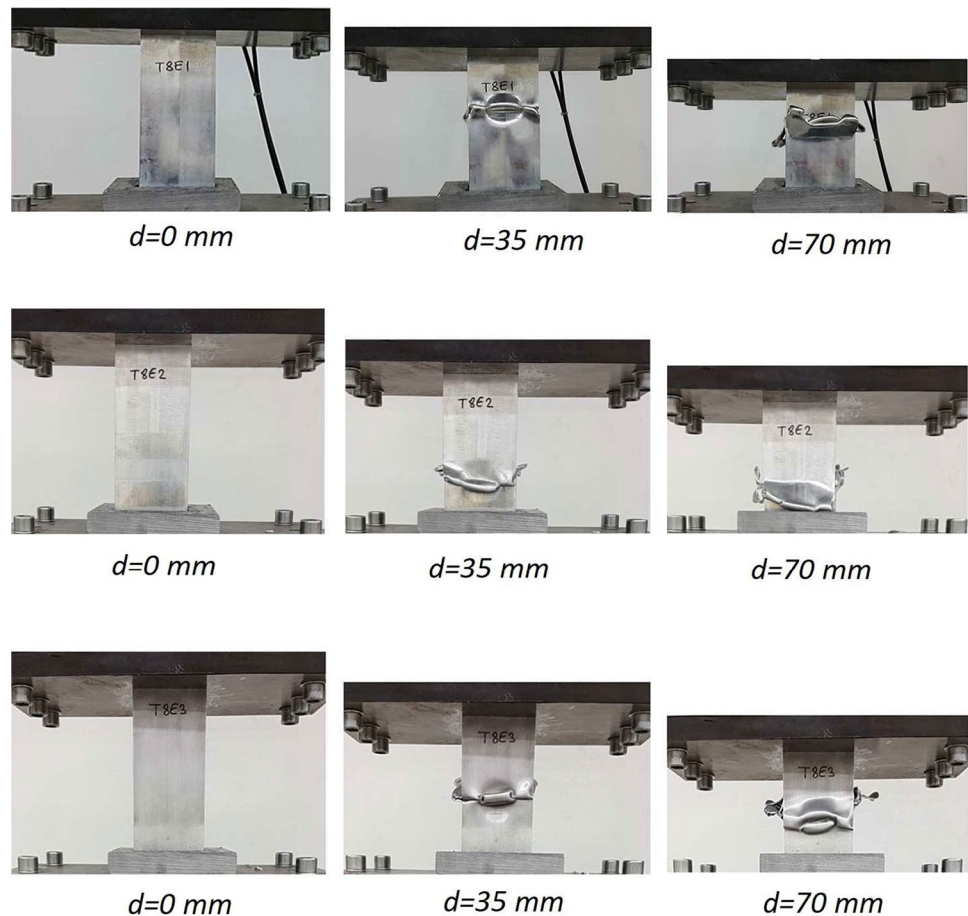


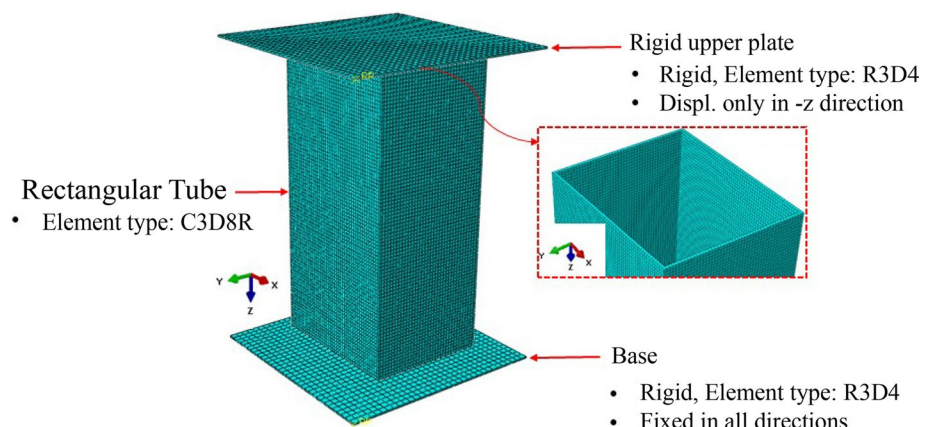
Fig. 7 Progressive failure behavior of multi-cell test specimens (T8E) at different stages: $d = 0$ mm, $d = 35$ mm, $d = 70$ mm **a** test specimen T8E1 **b** test specimen T8E2 **c** test specimen T8E3



(8-node linear brick) wherein reduced integration with hour-glass control was achieved. The finite element (FE) models of the Al 6061-T6 tube were subjected to axial loading, and both the upper and lower platens were modeled as rigid parts as shown in Fig. 8. The boundary conditions were set as follows: the upper rigid wall was allowed to move only along the height of the tube, and the lower one was constrained from all degrees of freedom. The general contact algorithm in ABAQUS/Explicit was adopted to model the contact

behavior between the rigid walls and the tube. The friction coefficient value of 0.3 and hard contact was used to represent the tangential behavior and the normal behavior penalty contact algorithm, respectively. This algorithm approximates the contact enforcement and also hard contact by applying penalty stiffness in ABAQUS. Also, it allows a small amount of penetration by adjusting the normal force–overclosure stiffness, automatically [26].

Fig. 8 Finite element analysis model of the single-cell and multi-cell tube



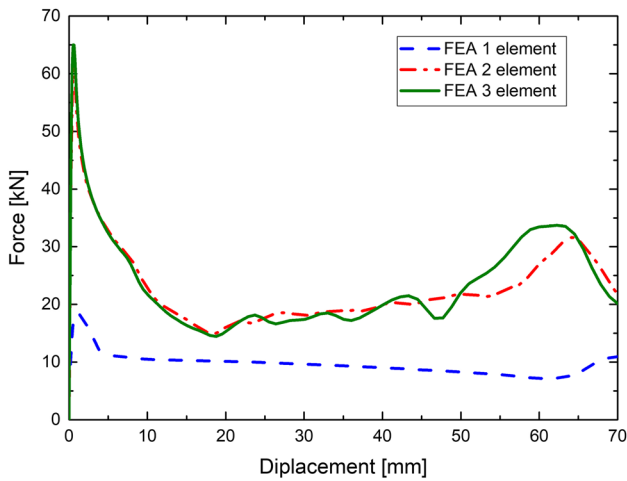


Fig. 9 Force–displacement behavior of the single-cell FE model with various number of elements through the wall thickness: blue, red, and green curves represent 1 element, 2 elements, and 3 elements through the thickness in FE model, respectively

Table 1 Convergence analyses based on the number of elements used in the thickness direction for single-cell tube

Number of elements through the thickness	IPF (kN)	SEA (kJ/kg)	E_a (kJ)	CFE (MCF/IPF)
1	18.3	3.04	0.69	0.535
2	62.5	7.21	1.63	0.372
3	66.2	7.35	1.66	0.358

The initial FE simulation showed that the computation time was excessively longer due to the high number of elements and nodes in the FE model. Therefore, a quarter model of the single-cell tube was developed and used in the computational study. A mesh convergence study based on the IPF and total energy absorption of the models for a cut-off distance of 70 mm was performed. Note that, an element size of 2 mm along the tube height was considered in all simulations. The force–displacement curves of the models with 1, 2, and 3 elements in the thickness directions are compared in Fig. 9, and the respective crash-worthiness results are presented in Table 1. Peak force was observed to be the most affected parameter by the number of elements used. Hou et al. [27] investigated the progressive crushing of honeycombs made of aluminum subjected to different loading conditions including the quasi-static one. In that study, the numerical model, in which shell elements were used for discretization of the workpiece material, did not successfully predict the IPF obtained experimentally. We believe that a model with

solid elements having enough number of elements in the thickness direction would give better results when compared with the tests. Note that this finding will be discussed in detail in Sect. 5. In our study, the FE model with 2 elements through the wall thickness was found to be appropriate in terms of optimizing the computational time with reasonable accuracy for the analysis.

4.2 Material model

The single-cell and multi-cell tubes were modeled using a linear elastic material model accompanied with J–C plasticity. The elastic properties are as follows: Young’s modulus is 68.9 GPa, Poisson’s ratio is 0.33, and material density is 2700 kg/m³. The J–C material parameters used in the FEM for the aluminum tube are listed in Table 2. In this table, A, B, C, n, and m are material constants; $\dot{\epsilon}$ is the strain rate; θ_{melt} is the melting temperature; and $\theta_{transition}$ is the transition temperature at which the transition from ductile to brittle fracture takes place.

The J–C damage model was used to characterize the failure behavior of the tube. It is an empirical model represented by the following equation:

$$\bar{\epsilon}_f^{pl} = \left[D_1 + D_2 \exp \left(D_3 \frac{\sigma_m}{\sigma_{eq}} \right) \right] \left[1 + D_4 \ln \frac{\dot{\epsilon}}{\dot{\epsilon}_0} \right] \left[1 + D_5 T^* \right], \tag{5}$$

where ϵ_f is the failure strain, σ_m/σ_{eq} is the stress triaxiality (η) as the ratio of the mean stress to the von Mises effective stress, $\dot{\epsilon}/\dot{\epsilon}_0$ is the dimensionless ratio of strain rates (with the latter reference value equal to 1.0 s⁻¹), T^* is the homologous temperature, and $D_i, i = 1, \dots, 5$ are the material constants. The parameters used in the FE model were $-0.77, 1.45, -0.47, 0, 1.6$ for $D_1, D_2, D_3, D_4,$ and D_5 , respectively [29].

As in the simulations quasi-static conditions were considered, the strain-rate and temperature effects were not significant; hence, the second and third terms in the above equation did not influence $\bar{\epsilon}_f^{pl}$. This is also valid for the J–C plasticity model explained above. Damage initiation occurs if the following condition is satisfied.

$$\int \frac{d\bar{\epsilon}^{pl}}{\bar{\epsilon}_f^{pl}(\eta)} = 1 \tag{6}$$

where $\bar{\epsilon}^{pl}$ is the equivalent plastic strain. The evolution of the damage following its initiation describes the progressive damage of the material. This is implemented using the displacement type linear softening law, where the evolution of the damage variable (d) is explained through the following equation:

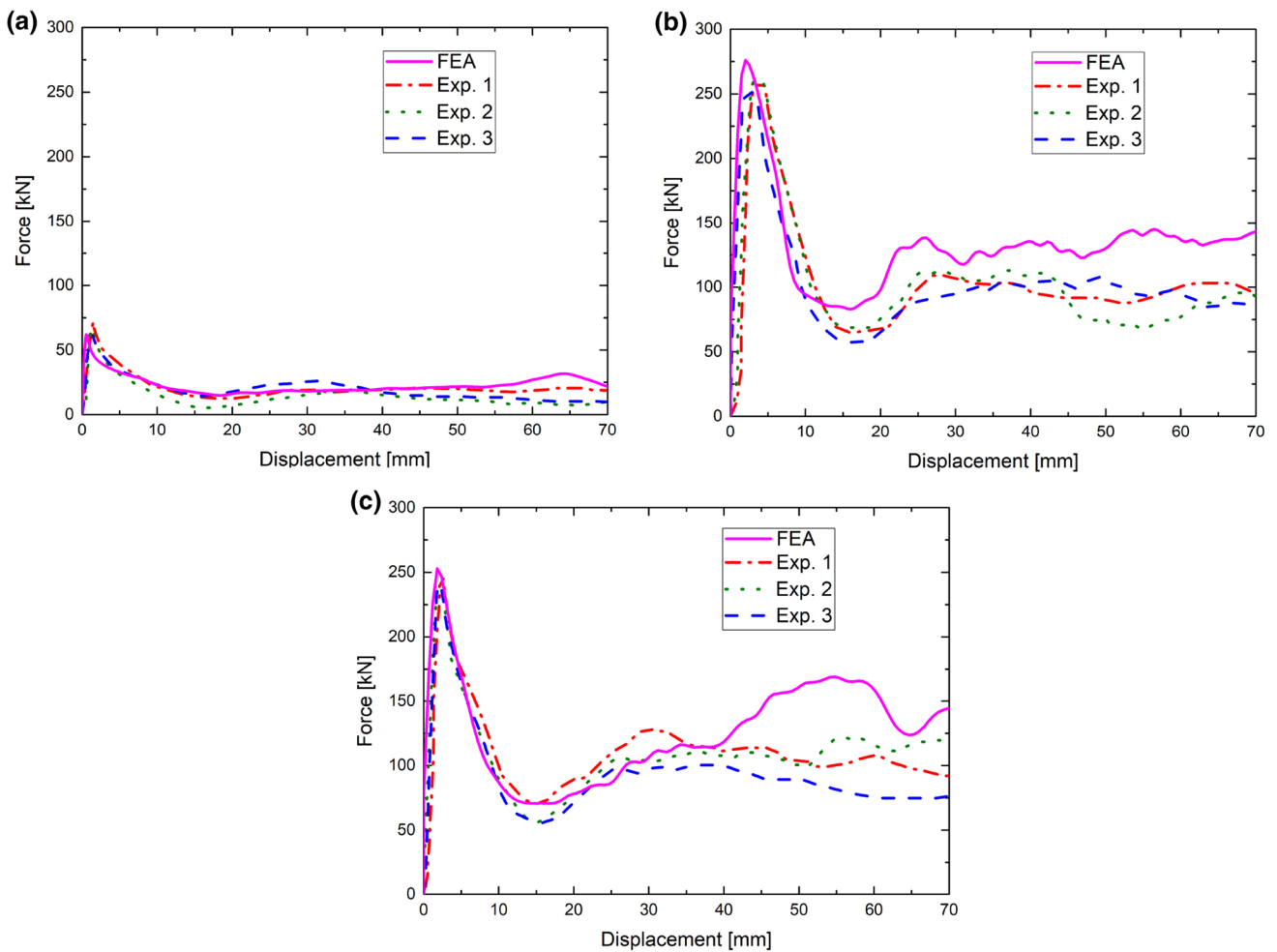


Fig. 10 Force–displacement behavior of test specimens from experiments and FEA **a** single-cell (T0) **b** multi-cell (T4E) **c** multi-cell (T8E): the results measured in the experiments are listed as (Exp1, Exp2 and Exp 3)

Table 2 The J–C material model of Al 6061-T6 used in numerical analyses [28]

A (MPa)	B (MPa)	n	C	m	$\dot{\epsilon}$ (s ⁻¹)	θ_{melt} (deg)	$\theta_{transition}$ (deg)
250	79.7	0.499	0.0249	1.499	1	583	300

$$\dot{d} = \frac{L_e \dot{\bar{\epsilon}}^{pl}}{\bar{u}_f^{pl}} = \frac{\dot{u}^{pl}}{\bar{u}_f^{pl}}, \tag{7}$$

where L_e is the element’s characteristic length, $\dot{\bar{\epsilon}}^{pl}$ is the equivalent plastic strain rate, and \bar{u}_f^{pl} is the effective plastic displacement at failure. When the effective plastic displacement (\bar{u}^{pl}) reaches \bar{u}_f^{pl} , a full degradation for the material

stiffness ($d = 1$) is reached, i.e., complete damage occurs; hence, the element is taken out from the mesh.

5 Comparison with experiments and sensitivity analysis of various parameters

In this part, the developed FE models are first compared with the experimental results presented in Sect. 3. Then, the energy absorption performance of the single-cell tube is predicted for various model parameters.

5.1 Validation of the FE model for single-cell and multi-cell tubes

The force–displacement curves of the single-cell tube and multi-cell tubes taken from the quasi-static experiments and FE simulations are presented in Fig. 10. A reasonable agreement between FEA and the experimental results was achieved. The crashworthiness results are compared in Table 3 for single-cell tube and multi-cell tubes (T4E, T8E). Table 3 presents a comparison of the FEA predictions and the experimental values. Columns 3, 5, 7 and 9 provide the percent error of the FEA predictions with respect to the average value (of three measurements) for the corresponding quantity. Columns 3, 5, 7 and 9 also provide the coefficient of variation of the corresponding quantity realized in the measurements. It is seen that the error in FEA predictions is acceptable compared to

the coefficient of variations realized in the experimental measurements.

The FEA results deviate from the experimental results by 25.6%, – 7.6%, 35.2%, and 21.7% for energy absorbed, IPF, CFE, and SEA for single-cell tube, respectively. The respective values for T4E specimens are 27.8%, 7.4%, 19.5%, and 26.4%. Moreover, they are 19.9%, 4.6%, 14.9%, and 16.9% for T8E specimens. Although the general trend of the force–displacement curves for the three different experimental results was similar, they deviated from each other significantly. Therefore, the errors resulting from FEA simulations were considered to be within an acceptable range. Note that, multi-cell tubes have better crashworthiness performance in terms of CFE and SEA when compared to single-cell tube, but they do not show significant difference for these two parameters when compared with each other.

The undeformed and deformed shapes of the single-cell tube, multi-cell tubes T4E and T8E obtained experimentally and numerically are presented in Figs. 11, 12 and 13, respectively. For the single-cell tube, the isometric and front views of the box are presented for a better comparison. They are observed to be similar, and the middle region of the tube undergoes severe plastic deformation with a single fold. The fracture occurring at the corners of the folded region was also captured successfully by the numerical model (see the encircled regions in Fig. 11). Here, it is worth mentioning the effect of type of elements used to model the single-cell

Table 3 Comparison of energy absorption performances of T0, T4E, and T8E test specimens and FE models: the results measured in the experiments are listed as Exp 1, Exp 2, and Exp 3

	E_d (kJ)	Error or C.o.v.	IPF (kN)	Error or C.o.v.	CFE	Error or C.o.v.	SEA (kJ/kg)	Error or C.o.v.
T0-FEA	1.63	25.6	62.5	– 7.6	0.372	35.2	7.21	21.7
T0-Exp 1	1.49	15.0	72.0	6.4	0.293	6.5	6.72	13.5
T0-Exp 2	1.01	– 22.1	68.0	0.4	0.212	– 22.9	4.55	– 23.2
T0-Exp 3	1.39	7.2	63.0	– 6.9	0.319	16.0	6.50	9.7
T0-Average	1.30	19.6*	67.7	6.7*	0.275	21.0*	5.92	20.2*
(SD)	(0.25)		(4.5)		(0.058)		(1.19)	
T4E-FEA	9.37	27.8	276.1	7.4	0.483	19.5	20.94	26.4
T4E-Exp 1	7.43	1.3	259.9	1.1	0.406	0.5	16.73	0.9
T4E-Exp 2	7.35	0.2	259.9	1.1	0.399	– 1.2	16.48	– 0.7
T4E-Exp 3	7.21	– 1.5	251.2	– 2.2	0.407	0.7	16.55	– 0.2
T4E-Average	7.33	1.5*	257.0	1.9*	0.404	3.2*	16.59	0.8*
(SD)	(0.11)		(5.0)		(0.013)		(0.13)	
T8E-FEA	8.90	19.9	252.7	4.6	0.500	14.9	20.08	16.9
T8E-Exp 1	7.84	5.6	246.4	1.9	0.451	3.7	18.02	4.9
T8E-Exp 2	7.89	4.9	238.0	– 1.4	0.462	6.2	18.07	5.2
T8E-Exp 3	6.63	– 10.5	240.5	– 0.4	0.393	– 9.6	15.44	– 10.0
T8E-Average	7.42	9.2*	241.6	1.8*	0.435	5.9*	17.18	8.9*
(SD)	(0.68)		(4.3)		(0.026)		(1.52)	

*% coefficient of variation: $100 \times \text{SD}/\text{Average}$

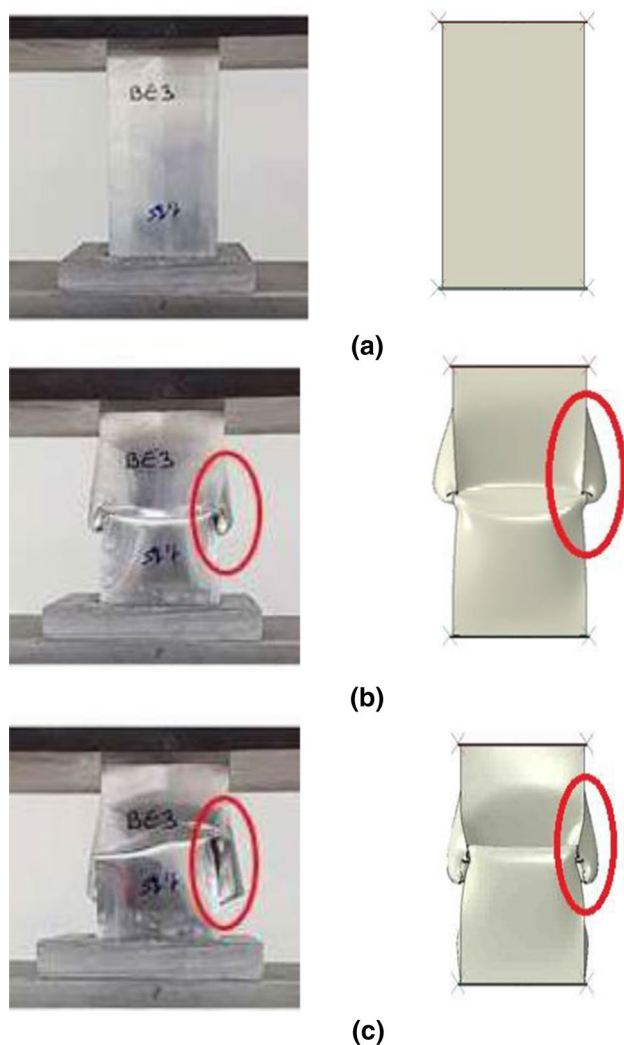


Fig. 11 Front (right) and isometric (left) deformed views of single-cell FE model and the test specimen at different stages: **a** $t = 0$ min **b** $t = 15$ min **c** $t = 30$ min

tube. Initially, shell elements were used to simulate the thin-walled tube and it was observed that they were not capable of capturing the deformation shape accurately. Similarly, Reddy et al. [30] showed the importance of damage model and solid elements usage in their numerical study. They improved the closeness of energy absorption results of simulations and experiments when they applied J–C damage model for aluminum alloy in their simulations. Energy absorption results of the FE model with solid elements and FE model with shell elements are compared in Table 4. The numerically obtained curves diverge from each other from the beginning of the deformation process as shown in Fig. 14. The reason why the shell elements showed worse results when compared to solid elements can be attributed to the deformation characteristics of the folding mechanism. It was observed that initial local buckling of the structure

started at the top of the tube where it first contacted by the rigid wall. Due to the local failure of the elements in this region consecutively, the tube absorbed more energy which is inconsistent with the experimental observations (see the 5–45 mm deformation region in Fig. 14)

When the crashworthiness metrics were compared, it was observed that the model accounting for the solid elements was in better agreement with the test results. The deformed shapes for different deformation levels are presented in Fig. 15. A noteworthy difference was observed from the beginning of the deformation. A better prediction of folding at the middle of the tube was obtained when the solid elements were considered instead of shell elements in the simulations. Using shell elements resulted in incorrect deformation pattern as observed in the force–displacement behavior given in Fig. 14. We believe that the reason for this was the rotational degree of freedom of the nodes at the top of the thin-walled tube during the initial contact with the rigid upper plate. Therefore, unrealistic multifolding was obtained with the model having shell elements. This might be avoided by constraining the rotational degree of freedom of the tube nodes that are in contact with the rigid walls although this is not considered to be a typical problem for shell elements.

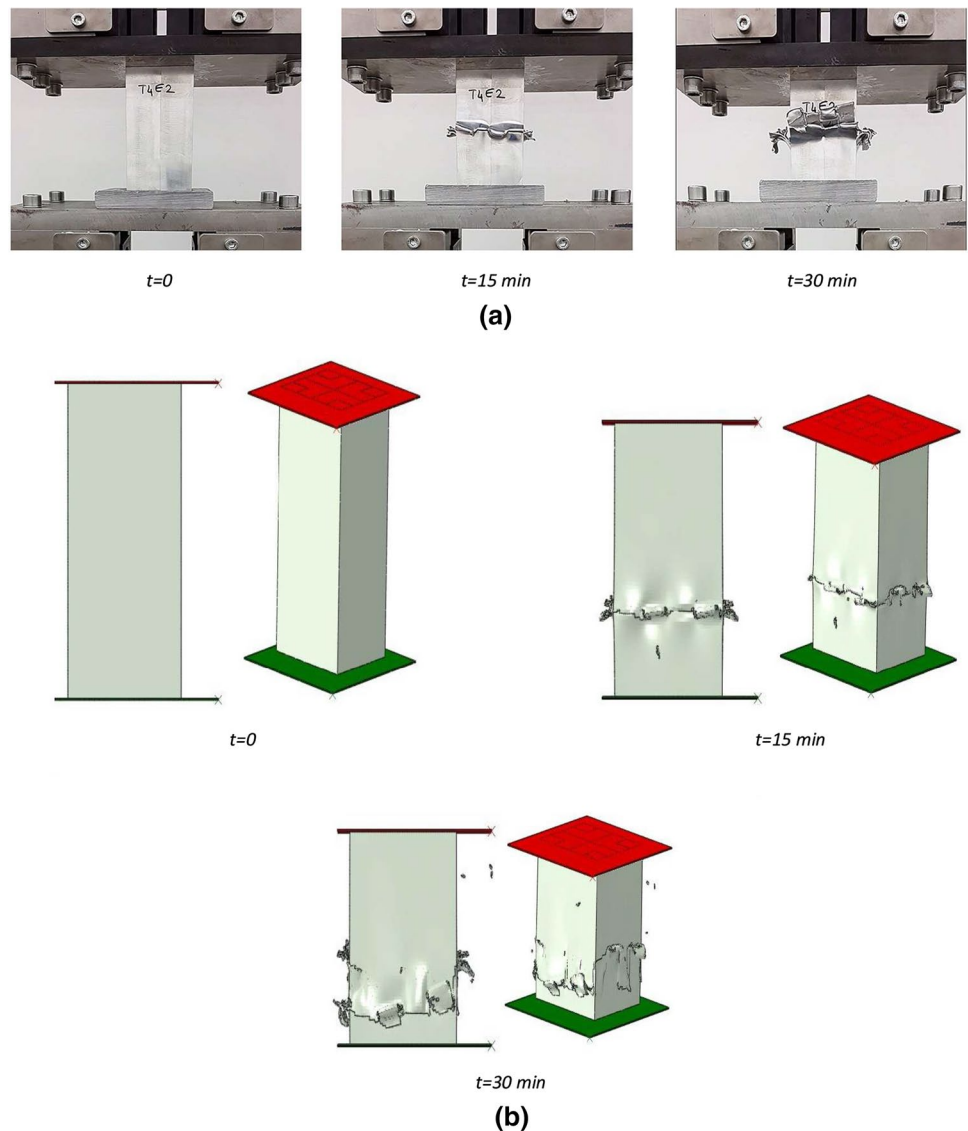
5.2 Prediction of the crashworthiness performance for various model parameters

There are various model parameters that may affect the crashworthiness performance of the crash tube, such as the height and wall thickness of the tube, material model used, and the velocity of the rigid upper plate. In this section, the single-cell model is chosen for the investigation of the effects of model parameters on the crashworthiness performance because of its less complexity. Herein, the average of the experimental results will be used as a reference for comparing the obtained results using FE analysis.

5.2.1 Effect of the tube height

Although various factors on the crashworthiness including the thickness of the tube, tube cross section were investigated, limited researchers focused on the effect of tube length on energy absorption performance. Zang et al. [31] analyzed the failure modes and energy absorption mechanisms and the effects of tube length, the thickness ratio of the aluminum alloy to the CFRP, the layer number, and the fiber sequence on the crashworthiness of the CFRP/aluminum alloy hybrid tubes. Similarly, Zarei and Kroeger [32] dealt with experimental and numerical investigations of square and hexagonal composite tubes and studied the effect of tube length. Impact tests were conducted on composite tubes and thin shell elements were used to model the tube.

Fig. 12 Front (left) and isometric (right) views of multi-cell T4E tube at different stages: $t = 0$ min, $t = 15$ min, $t = 30$ min **a** test specimen **b** FE model



To examine the influence of the tube height of the single-cell tube on the energy absorption and deformation shapes, FE simulations were carried out with a thickness of 1.5 mm and heights of 120, 150, 180, and 210 mm. The respective force–displacement graphs and crashworthiness results are shown for the half length of the tubes in Fig. 16 and Table 5, respectively. The energy absorption performances of each tube for the deformation distances are given in detail. As the tube height was increased from 120 to 210 mm, the IPF decreased from 72.6 to 60.3 kN and the total energy absorption increased from 1.33 to 2.17 kJ. However, the relationship between the height and other metrics were found to be complex. For instance, CFE decreased with an increase in the tube height except for the one with 120 mm height.

Figure 17 presents the deformed views of the tubes having different heights when they are deformed up to their mid-heights. While double folding was observed for the

highest tube, a single folding occurred for the others. Figure 16 shows that the initial folding occurs when the rigid upper plate traveled approximately 55 mm, 67 mm, 65 mm, and 60 mm for the shortest to the longest tubes, respectively. Considering the height of the samples, a folding occurs at 0.45, 0.44, 0.36, and 0.28 of their heights, respectively. It was concluded that the longer tubes had a tendency to undergo a greater number of folding, and it occurred at smaller deformation levels with respect to their heights.

5.2.2 Effect of the wall thickness

To explore the impact of the wall thickness on the crashworthiness of the aluminum tubes, FE simulations were carried out with tubes having thickness of 1, 1.5, and 2 mm and a height of 180 mm. The force–displacement curves and

Fig. 13 Front (left) and isometric (right) views of multi-cell T8E tube at different stages: $t = 0$ min, $t = 15$ min, $t = 30$ min **a** test specimen **b** FE model

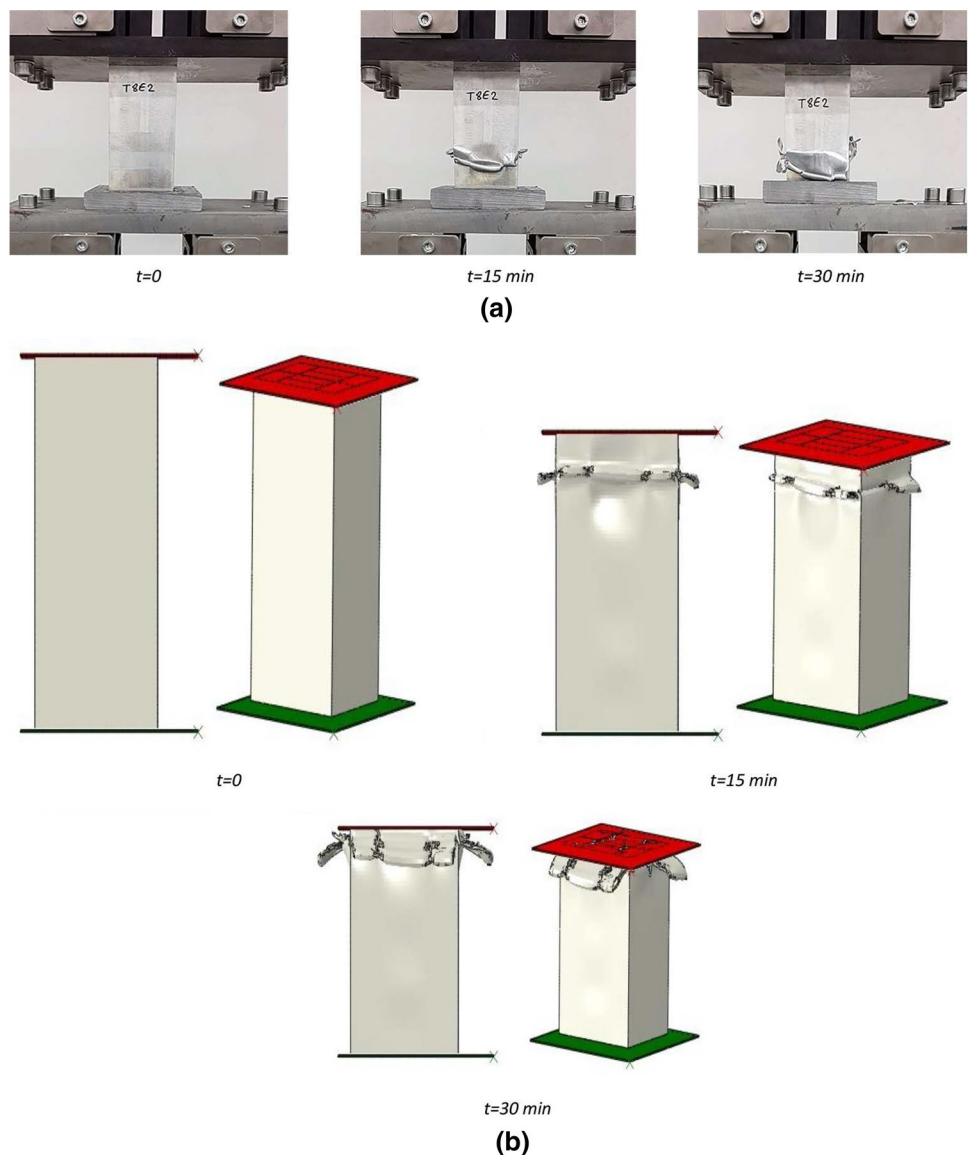


Table 4 Comparison of crashworthiness metrics in cases with shell elements and with solid elements for single-cell tube: average corresponds to the average of three experimental results

	E_a (kJ)	Error or C.o.v.	IPF (kN)	Error or C.o.v.	CFE	Error or C.o.v.	SEA (kJ/kg)	Error or C.o.v.
T0-Average (SD)	1.30 (0.25)	19.6*	67.7 (4.5)	6.7*	0.275 (0.058)	21.0*	5.92 (1.19)	20.2*
Solid Elements	1.63	25.6	62.5	- 7.6	0.372	35.2	7.21	21.7
Shell Elements	2.06	58.8	50.7	- 25.1	0.579	110.5	9.12	53.9

(*)% coefficient of variation: $100 \times \text{st.dev.} / \text{Average}$

crashworthiness results are depicted in Fig. 18 and Table 6, respectively. With an increase in the wall thickness, the IPF increased from 29.5 to 106.9 kN, the total energy absorption increased from 0.83 to 2.54 and the SEA increased from 5.45 to 8.48 kJ/kg for the thinnest and the thickest tube, respectively. An increase in the tube thickness results

in an increase in its volume and mass; hence, the observed changes in these metrics are in line with the expectations. Especially, the increased SEA for the thicker tubes proved their better performance. However, a decrease in the CFE was observed for the respective tubes.

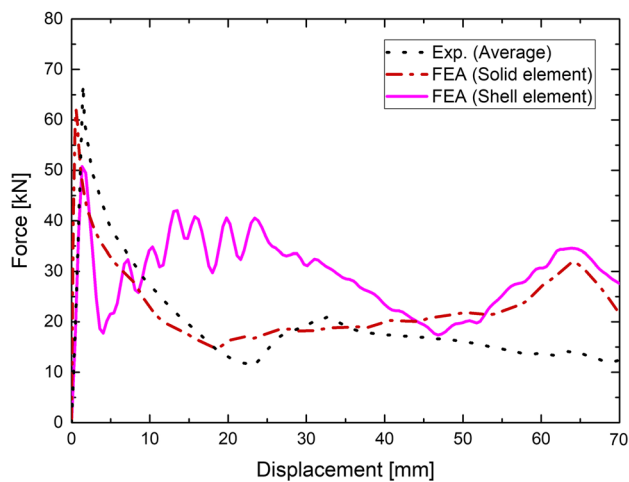


Fig. 14 Force–displacement behavior of single-cell tubes with shell elements and with solid elements: average corresponds to the average of three experimental results

The deformed shapes of the single-cell tubes obtained from FEA for wall thicknesses of 1, 1.5, and 2 mm are presented in Fig. 19. Firstly, all the tubes folded from their mid-heights. However, the deformed shapes are similar for the two thicker geometries ($t = 1.5$ and $t = 2$ mm) and different for the thinnest one ($t = 1$ mm). The folding occurred in two directions and in one direction for the former and latter cases, respectively. It appeared that for the thicker tubes, the material volume could not bifurcate in one direction. Hence, semi-folding occurred in two directions since bifurcation in one direction requires more energy compared to the bifurcation in two directions.

5.2.3 Effect of failure parameters

In this section, we investigate how the deformation shape of the tube was affected when the damage was accounted for in the constitutive equations. FE simulations were conducted with and without the J–C failure model. The force–displacement behavior and crashworthiness results are presented in Fig. 20 and Table 7, respectively.

The numerically obtained curves depicted a very similar characteristic at the beginning, but they started to diverge from each other with the onset of damage as a result of the increase in deformation. When the crashworthiness metrics were compared, it was observed that the model accounting for the damage was in slightly better agreement with the test results. The deformed shapes at two different deformation levels are presented in Fig. 21. Although they looked similar when the rigid upper plate travelled 15 mm, a noteworthy difference was observed when it travelled one-third of the tube height (60 mm). On comparison with Fig. 11, it was concluded that the model accounting for the damage

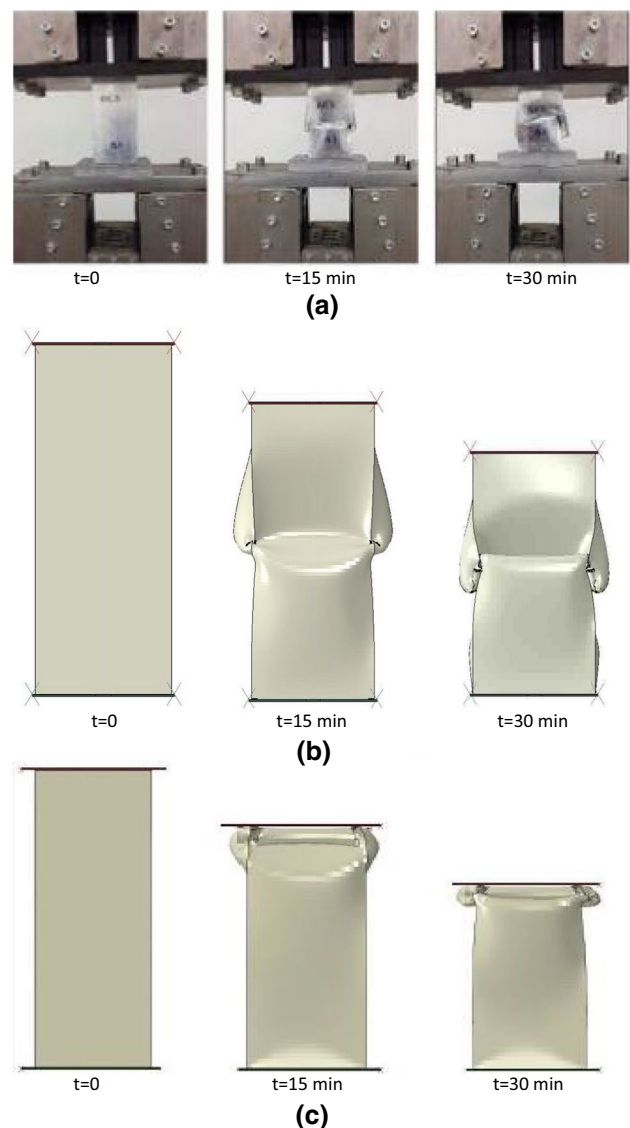


Fig. 15 Front views of single-cell FE model and the test specimen at different stages: $t = 0$ min, $t = 15$ min, $t = 30$ min **a** experiments **b** solid elements **c** shell elements

law in the constitutive equations predicted the folding pattern observed in the experiments more accurately than the one that did not account for the damage law. This observation was also reported by Qiao et al. [17] who examined the impact of damage parameters on the crashworthiness of square aluminum tubes. They concluded that a better prediction of folding was attained when the geometric imperfection and damage evolution were considered in the simulations.

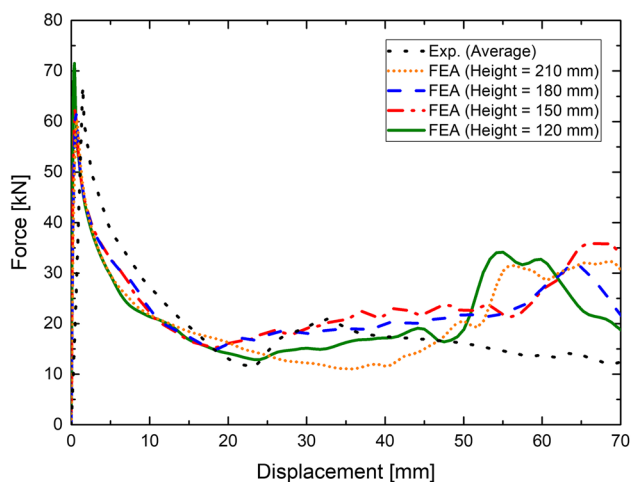


Fig. 16 Force–displacement behavior of the single-cell tubes with different heights: average corresponds to the average of three experimental results

Table 5 Comparison of crashworthiness metrics for various tube heights for single-cell tube

Tube height (mm)	Deformation (mm)	E_a (kJ)	IPF (kN)	CFE	SEA (kJ/kg)
120	60	1.33	72.6	0.302	8.79
150	75	1.87	62.2	0.399	9.94
180	90	2.02	62.5	0.356	7.21
210	105	2.17	60.3	0.342	8.24

6 Optimization

In this study, the single-cell and multi-cell tubes are optimized for maximum CFE and maximum SEA. The main difficulty in optimization is related with the huge computational cost of crash simulations. A single crash simulation

takes hours to complete even with high computational power. To overcome this difficulty, the use of surrogate models has been explored by several researchers to perform crashworthiness optimization of the tubes [33–44]. In this study, we also follow a surrogate-based optimization approach detailed below.

6.1 Definition of the optimization problem

In this study, the thin-walled tubes are designed to attain the maximum value of the following two metrics: CFE and SEA. For all T0, T4E, and T8E designs, the wall thickness and the tube length are chosen as the design variables. Thus, optimization problem for maximum CFE (or maximum SEA) can be stated as

$$\begin{aligned} \text{Min} \quad & -\text{CFE}(\text{or } -\text{SEA}) \\ \text{s.t.} \quad & 1 \text{ mm} \leq t \leq 2 \text{ mm} \\ & 150 \text{ mm} \leq L \leq 210 \text{ mm} \end{aligned} \tag{8}$$

The optimization problems defined above are solved by using “ga” built-in function of MATLAB that uses genetic algorithm [45]. The optimization problems defined above are solved by using “ga” built-in function of MATLAB that uses genetic algorithm. The population size is taken 100, the elite count is taken 6, the crossover fraction is taken 80%, the maximum number of generations is taken 300, and remaining algorithms parameters are taken as the default values in MATLAB.

Since calculations of CFE and SEA require computationally intensive FE simulations, optimization using genetic algorithm is challenging. In this case, surrogate models offer a practical solution.

Fig. 17 Deformed views of the single-cell tubes obtained from FEA with different heights **a** height = 120 mm **b** height = 150 mm **c** height = 180 mm **d** height = 210 mm: x represents the deformed distance of the tube (mid-height)

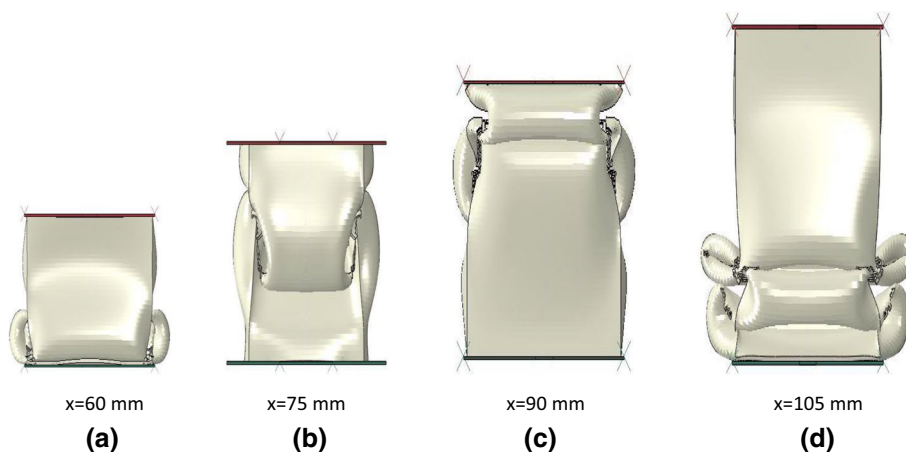
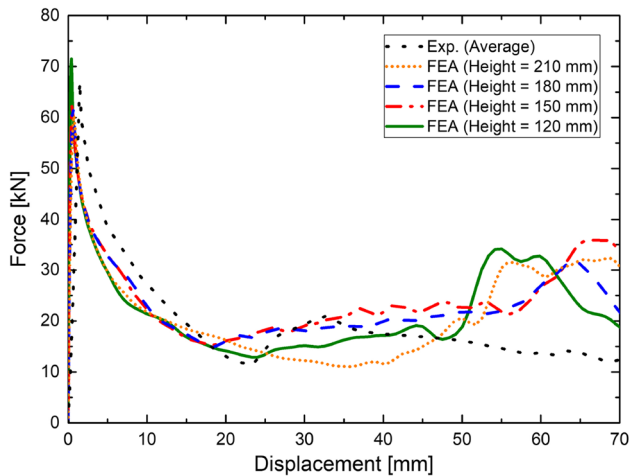


Table 6 Comparison of crashworthiness metrics for various tube thicknesses for single-cell tube

Tube thickness (mm)	E_{absorbed} (kJ)	IPF (kN)	CFE	SEA (kJ/kg)
1	0.83	29.5	0.400	5.45
1.5	1.63	62.5	0.372	7.21
2	2.54	106.9	0.338	8.48

**Fig. 18** Force–displacement behavior of the single-cell tubes with different thicknesses: average corresponds to the average of three experimental results

6.2 Construction of surrogate models

Surrogate models provide regression or interpolation fitting of the responses evaluated at some training points. Surrogate model construction is performed at four steps. First, some training points are determined for the input variables based on a design of experiments (DOE) technique. Second, the responses are evaluated corresponding to the training

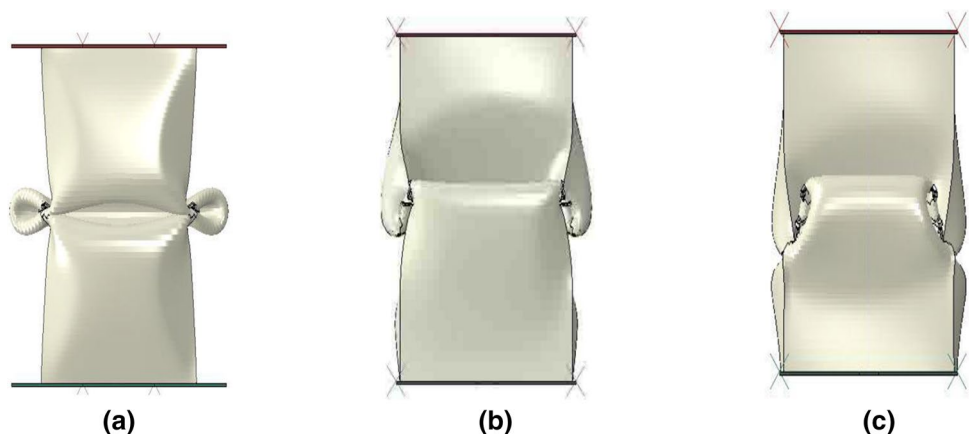
points. Third, a surrogate model is fit (that is, mathematical relationship is assessed between the input variables and the responses) by using the training point matrix and the corresponding response vector. Finally, the accuracy of the surrogate model is evaluated. The constructed surrogate model can be used to estimate the response at any arbitrary point in the input variable space.

6.2.1 Design of experiments

In this study, we use Latin hypercube sampling (LHS) design of experiments technique to generate the training points [46–48]. The reader is referred to the Appendix A of Acar et al. [49] for brief details of generate the training points through LHS. The sample size of the training points is in accordance with the suggestion of ten times the number of variables proposed by Jones et al. [50]. Since the number of variables is two, we generated 20 training points. Then, the responses corresponding to these training points are evaluated through FEA.

6.2.2 Fitting surrogate models

There exists different types of surrogate models available in the literature including polynomial response surfaces [48, 51], Kriging [52, 53], radial basis functions [54, 55], neural networks [56], support vector regression [57], etc. In this study, we use quadratic response surface (QRS) surrogate, and Kriging surrogate with first order trend model and Gaussian correlation model (KR1) as different types of surrogate models. The reader is referred to the Appendix B of Acar et al. [49] for brief details of the mathematical formulations of QRS and KR1.

Fig. 19 Deformed views of the single-cell tubes at 60 mm displacement of the rigid upper plate for various values of quarter tube thicknesses **a** $t = 1$ mm **b** $t = 1.5$ mm **c** $t = 2$ mm

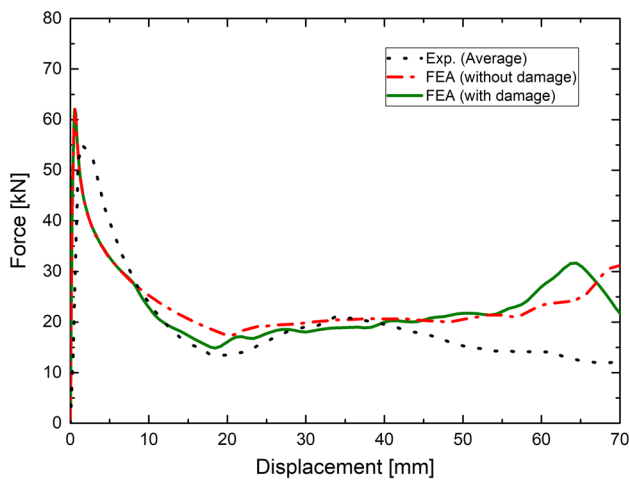


Fig. 20 Force–displacement behavior of the single-cell tubes with and without damage model: average corresponds to the average of three experimental results

6.2.3 Accuracy of surrogate models

The accuracies of the constructed surrogate models are evaluated using leave-one-out generalized mean square cross validation error metric, GMSE. The GMSE is calculated as follows. If there are N training points, a surrogate model type is constructed N times, each time leaving out one of the training points. Then, the difference between the exact value of the response y_k at the omitted training point x_k and the predicted value of the response using the surrogate model $\hat{y}_k^{(-k)}$ is calculated. Finally, GMSE is calculated from

$$GMSE = \sqrt{\frac{1}{N} \sum_{k=1}^N (\hat{y}_k^{(-k)} - y_k)^2} \tag{9}$$

GMSE values can be normalized with respect to the mean values of responses evaluated at training points as follows:

Table 7 Comparison of crashworthiness metrics in cases with and without damage model for single-cell tube

	E_a (kJ)	Error or C.o.v.	IPF (kN)	Error or C.o.v.	CFE	Error or C.o.v.	SEA (kJ/kg)	Error or C.o.v.
T0-Average (SD)	1.30 (0.25)	19.6*	67.7 (4.5)	6.7*	0.275 (0.058)	21.0*	5.92 (1.19)	20.2*
With Damage	1.63	25.6	62.5	− 7.6	0.372	35.2	7.21	21.7
Without Damage	1.64	26.6	62.5	− 7.6	0.375	36.4	7.27	22.7

(*)% coefficient of variation: $100 \times SD/average$

Fig. 21 Deformed views of single-cell tubes for $x = 15$ and $x = 60$ mm deformation **a** without damage **b** with damage

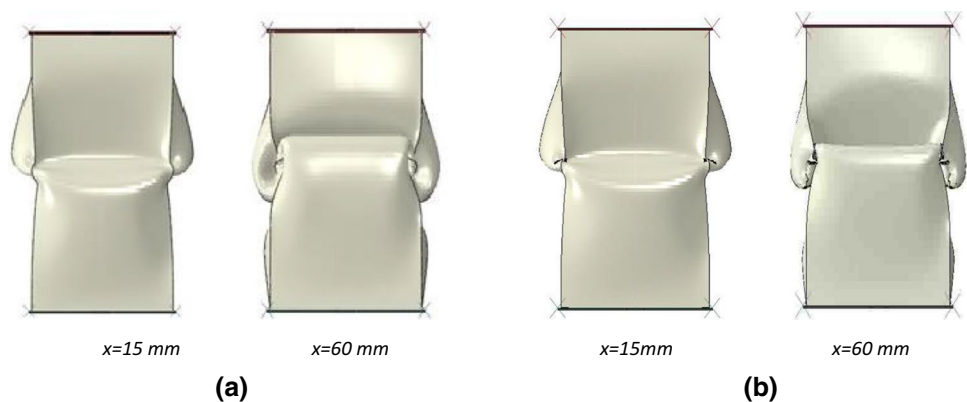
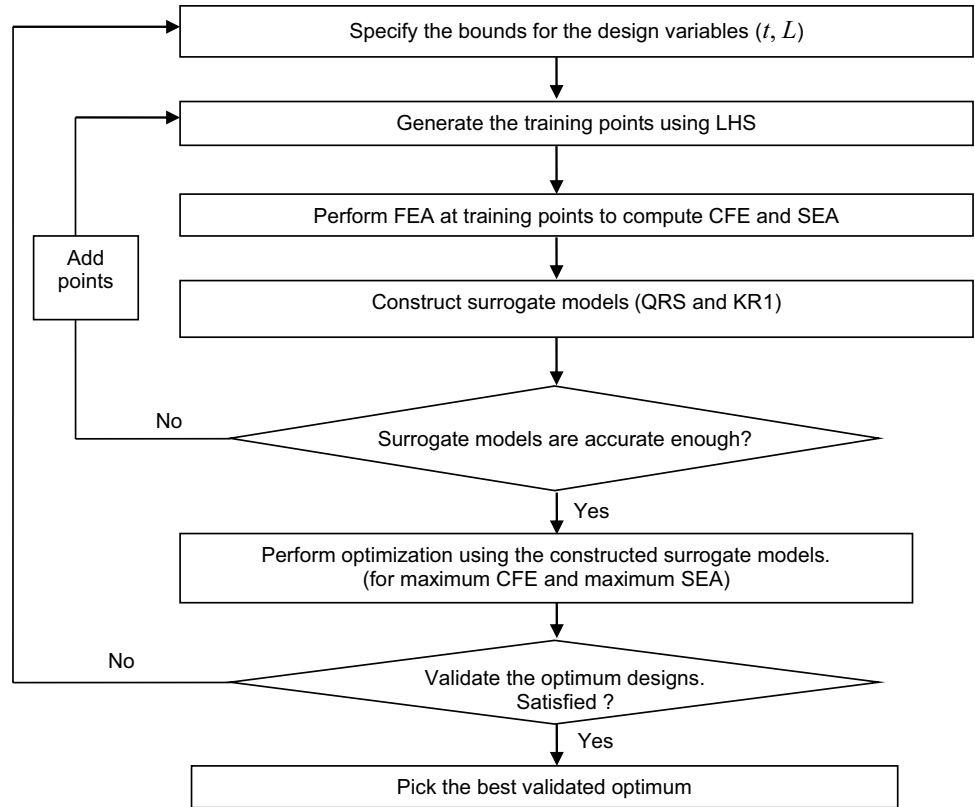


Table 8 Accuracies of surrogate models assessed by the normalized GMSE % values for tubes with T0, T4E, and T8E designs

Design	T0		T4E		T8E	
	CFE	SEA	CFE	SEA	CFE	SEA
QRS	4.28	2.53	4.19	4.62	8.16	9.22
KR1	3.99	3.44	4.15	4.22	9.88	9.21

Bold values show the most accurate model

Fig. 22 Flowchart for surrogate-based crashworthiness optimization of the single and multi-cell tubes



$$GMSE_{nor} = \frac{GMSE}{\frac{1}{N} \sum_{k=1}^N y^k} \tag{10}$$

Table 8 provides the comparison of the $GMSE_{nor}$ of the surrogate models constructed for CFE and SEA prediction of the T0, T4E, and T8E designs. Table 8 shows that the QRS model is the most accurate model for the SEA prediction of the T0 design and the CFE prediction of the T8E design, whereas KR1 is the most accurate model for the remainder of the predictions.

6.3 Surrogate-based optimization with multiple surrogate models

In an earlier study, we showed that the optimum solution is not necessarily obtained by using the most accurate surrogate model [49]. Therefore, the tubes are optimized by using QRS and KR1 separately and the design with the optimum performance is determined. A flowchart showing the steps followed while performing surrogate-based optimization of the tubes is shown in Fig. 22.

Table 9 Optimization results for tubes with T0, T4E, and T8E designs

Design	Objective	Surrogate	t (mm)	L (mm)	CFE	SEA (kJ/kg)
T0	CFE	KR1	1.0	184.7	0.454	6.17
	SEA	QRS	2.0	194.2	0.343	8.63
T4E	CFE	QRS	2.0	210.0	0.590	27.0
	SEA	QRS	2.0	210.0	0.590	27.0
T8E	CFE	KR1	1.7	156.3	0.544	24.5
	SEA	KR1	1.7	194.2	0.542	24.6

6.4 Optimization results

Table 9 provides optimization results for T0, T4E, and T8E designs. Table 9 indicates that the maximum CFE and SEA values that can be attained by T4E designs are larger than those of the T8E designs, which are substantially larger than those of the T0 designs.

For T0 designs, the tube thickness should take its minimum value (i.e., 1 mm) for maximum CFE, whereas it should take its maximum value (i.e., 2 mm) for maximum SEA. It is also seen for T0 designs that the tube length of the optimum CFE design is slightly smaller than that of the optimum SEA design.

For T4E designs, both the tube thickness and the tube length should take their corresponding maximum values (i.e., 2 mm and 210 mm, respectively) to attain both maximum CFE, and maximum SEA.

For T8E designs, the optimum values of the tube thickness and the tube length for maximum CFE are slightly larger than those required for maximum SEA.

7 Conclusions

In this study, the crashworthiness of single-cell and multi-cell aluminum tubes subjected to quasi-static conditions was studied experimentally and numerically. All the specimens folded at their mid-heights in the tests conducted. The J–C material model with its complementary damage model was used to characterize the material behavior of the tubes during the deformation in the numerical model. The crashworthiness performances of the single-cell and multi-cell tubes were evaluated using different metrics such as energy absorbed, specific energy absorption, initial peak force, and crush force efficiency. Furthermore, a parametric study was performed on the single-cell model to see the effect of model parameters such as tube height, wall thickness, failure parameters and velocity. Moreover, surrogate-based optimization of the single cell tubes (T0) and two different types of multi-cell tubes (T4E, T8E) is performed to maximize crush force efficiency (CFE) and specific energy absorption (SEA). From this study, the following conclusions can be drawn.

- Solid elements were observed to be more successful in modeling the crush behavior of thin-walled aluminum tubes when compared to the shell elements. Also, the number of elements in the thickness direction significantly influenced the initial peak load.
- Both of the multi-cell tube designs performed much better than single-cell tubes in terms of CFE and SEA.
- When the height of the tube was increased, there was a high chance of getting more folds at earlier deformation

levels. Consequently, the tube could not absorb the energy efficiently; however, the initial peak load decreased.

- With an increase in the thickness of the tube, the fold could not evolve completely in one direction; instead, it was followed by another fold in a direction normal to that of the first fold. However, an increase in the velocity of the rigid upper plate prevented the formation of the second fold.
- When the damage law was accounted for in the constitutive equations, the response of a tube under compression loading was better predicted compared to that using only the elasto-plastic material model.
- Maximum CFE and SEA values that can be attained by T4E designs are larger than those of the T8E designs, which are substantially larger than those of the T0 designs.

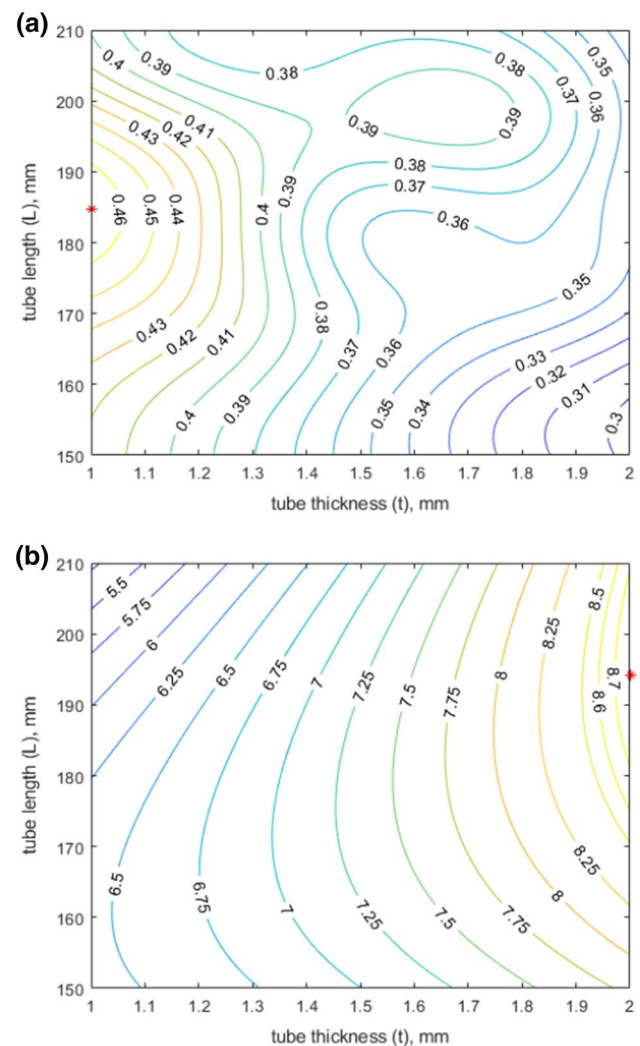


Fig. 23 Optimum tube thickness (t) and tube length (L) for T0 design obtained by using graphical optimization method, where the contour data are generated using KR1 model for CFE prediction, and using QRS model for SEA prediction

Table 10 Optimization results for T0, T4E, and T8E designs obtained by using QRS

Design	Objective	t (mm)	L (mm)	CFE (pred)	SEA (kJ/kg) (pred)	CFE (FEA)	SEA (kJ/kg) (FEA)	% error in CFE	% error in SEA
T0	CFE	1.0	164.8	0.453	6.43	0.449	6.29	0.9	2.3
	SEA	2.0	194.2	0.359	8.79	0.343	8.63	4.7	1.9
T4E	CFE	2.0	210.0	0.607	27.7	0.590	27.0	2.9	2.8
	SEA	2.0	210.0	0.607	27.7	0.590	27.0	2.9	2.8
T8E	CFE	1.0	210.0	0.601	21.7	0.534	24.5	12.3	15.1
	SEA	2.0	150.0	0.577	25.7	0.504	22.8	14.5	12.8

Table 11 Optimization results for T0, T4E, and T8E designs obtained by using KR1

Design	Objective	t (mm)	L (mm)	CFE (pred)	SEA (kJ/kg) (pred)	CFE (FEA)	SEA (kJ/kg) (FEA)	% error in CFE	% error in SEA
T0	CFE	1.00	184.7	0.468	6.35	0.454	6.17	2.9	3.0
	SEA	2.00	185.9	0.345	8.67	0.341	8.51	1.1	1.9
T4E	CFE	1.90	210.0	0.605	25.8	0.584	26.3	3.5	-1.8
	SEA	1.85	203.7	0.587	26.6	0.583	26.9	0.8	-1.0
T8E	CFE	1.70	156.3	0.549	24.3	0.544	24.5	0.8	-0.9
	SEA	1.75	194.2	0.534	24.9	0.542	24.6	-1.4	1.5

- CFE of the optimum T4E design is 8.5% greater than CFE of the optimum T8E design and 30% greater than CFE of the optimum T0 design.
- SEA of the optimum T4E design is 9.8% greater than SEA of the optimum T8E design and 213% greater than SEA of the optimum T0 design.

Appendix: Details on optimization results

This section provides some details on optimization results for design problem stated in Eq. (8). Note that graphical optimization method can also be used to find the optimum values of the tube thickness (t) and tube length (L) instead of using genetic algorithm, because Eq. (8) is a design optimization problem with two design variables. In graphical optimization method, the optimum solution is obtained by drawing contours of the objective function. For illustration, optimization of T0 design for maximum CFE is shown in Fig. 23a, and optimization of T0 design for maximum SEA is shown in Fig. 23b. Note that the contour data of Fig. 23a are generated by using KR1 model, and that of Fig. 23b is generated by using QRS model. Notice that by using graphical optimization method, it was possible to confirm the optimum solutions found through genetic algorithm.

Tables 10 and 11 show the optimum results obtained by using QRS and KR1 models, respectively. We notice that even though KR1 models are globally more accurate than QRS models for CFE and SEA prediction of the T4E design, optimum tube designs obtained by using QRS models have

better CFE and SEA values than optimum tube designs obtained by using KR1 models. Similarly, optimum T8E design obtained by using KR1 model has larger CFE value than the optimum design obtained by using QRS model, even though PRS model is globally more accurate than KR1 model for CFE prediction of the T8E design. The underlying reason for these findings is that the globally most accurate model does not necessarily display the best performance locally (e.g., near the optimum).

Acknowledgements The experimental results obtained in this paper is from the research project which was supported by TUBITAK (the Scientific and Technological Research Council of Turkey) under the ARDEB-1002 Program (Project Number 115M025).

Compliance with ethical standards

Conflict of interest The authors declare that they have no conflict of interest.

References

1. Fu B, Liao C, Xie L, Li Z, Shu R (2020) A theoretical analysis on crush characteristics of corrugated tube under axial impact and experimental verification. *J Braz Soc Mech Sci Eng* 42(10):1
2. Demirci E, Yıldız AR (2018) An experimental and numerical investigation of the effects of geometry and spot welds on the crashworthiness of vehicle thin-walled structures. *Mater Test* 60(6):553
3. Paygozar B, Sadigh MS (2020) Practicability of metallic hybrid systems in enhancing the energy absorption capacity: expansion and buckling mechanisms. *J Braz Soc Mech Sci Eng* 42:1

4. Demirci E, Yıldız AR (2018) An experimental and numerical investigation of the effects of geometry and spot welds on the crashworthiness of vehicle thin-walled structures. *Mater Test* 60(7–8):661
5. Guler MA, Cerit ME, Bayram B, Gerceker B, Karakaya E (2010) The effect of geometrical parameters on the energy absorption characteristics of thin-walled structures under axial impact loading. *Int J Crashworth* 15(4):377
6. Rouzegar J, Assaee H, Elahi SM, Asiaei H (2018) Axial crushing of perforated metal and composite-metal tubes. *J Braz Soc Mech Sci Eng* 40(7):349
7. Hu D, Wang Y, Song B, Wang Y (2018) Energy absorption characteristics of a foam-filled tri-tube under axial quasi-static loading: experiment and numerical simulation. *Int J Crashworth* 23(4):417
8. Attar AA, Rasouli S, Chahardoli S (2020) Effect of combined multi-cell columns and exterior stiffeners on energy absorption parameters of thin-walled tubes under axial load. *J Braz Soc Mech Sci Eng* 42(9):1
9. Baykasoglu C, Cetin MT (2015) Energy absorption of circular aluminium tubes with functionally graded thickness under axial impact loading. *Int J Crashworth* 20(1):95
10. Sarkabiri B, Jahan A, Rezvani MJ (2017) Crashworthiness multi-objective optimization of the thin-walled grooved conical tubes filled with polyurethane foam. *J Braz Soc Mech Sci Eng* 39(7):2721
11. Altin M, Güler MA, Mert SK (2017) The effect of percent foam fill ratio on the energy absorption capacity of axially compressed thin-walled multi-cell square and circular tubes. *Int J Mech Sci* 131:368
12. Altin M, Acar E, Güler M (2018) Foam filling options for crashworthiness optimization of thin-walled multi-tubular circular columns. *Thin Walled Struct* 131:309
13. Yıldız AR, Abderazek H, Mirjalili S (2020) A comparative study of recent non-traditional methods for mechanical design optimization. *Arch Comput Methods Eng* 27:1031–1048
14. Li Z, Chen R, Lu F (2018) Comparative analysis of crashworthiness of empty and foam-filled thin-walled tubes. *Thin Walled Struct* 124:343
15. Kim SB, Huh H, Lee G, Yoo J, Lee M (2008) Design of the cross section shape of an aluminum crash box for crashworthiness enhancement of a car. *Int J Mod Phys B* 22(31n32):5578
16. Reyes A, Langseth M, Hopperstad OS (2003) Square aluminum tubes subjected to oblique loading. *Int J Impact Eng* 28(10):1077
17. Qiao J, Chen J, Che H (2006) Crashworthiness assessment of square aluminum extrusions considering the damage evolution. *Thin Walled Struct* 44(6):692
18. Marzbanrad J, Keshavarzi A, Aboutalebi FH (2014) Influence of elastic and plastic support on the energy absorption of the extruded aluminium tube using ductile failure criterion. *Int J Crashworth* 19(2):172
19. Allahbakhsh H, Saemi J, Hourali M (2011) Design optimization of square aluminium damage columns with crashworthiness criteria. *Mechanics* 17(2):187
20. Estrada Q, Szwedowicz D, Silva-Aceves J, Majewski T, Vergara-Vazquez J, Rodriguez-Mendez A (2017) Crashworthiness behavior of aluminum profiles with holes considering damage criteria and damage evolution. *Int J Mech Sci* 131:776
21. Estrada Q, Szwedowicz D, Rodriguez-Mendez A, Gómez-Vargas OA, Elias-Espinosa M, Silva-Aceves J (2018) Energy absorption performance of concentric and multi-cell profiles involving damage evolution criteria. *Thin Walled Struct* 124:218
22. Hooputra H, Gese H, Dell H, Werner H (2004) A comprehensive failure model for crashworthiness simulation of aluminium extrusions. *Int J Crashworth* 9(5):449
23. Estrada Q, Szwedowicz D, Baltazar M, Cortes C, Majewski T, Estrada CA (2016) The performance of energy absorption in structural profiles with different discontinuities. *Int J Adv Manuf Technol* 84(5–8):1081
24. Hughes TJ, Liu WK (1981) Nonlinear finite element analysis of shells-part II. Two-dimensional shells. *Comput Methods Appl Mech Eng* 27(2):167
25. Jirawattanakasem P, Bureerat S (2010) Effect of bearing sleeve lead-in chamfer, and parallelism on tolerance ring installation. *Eng Appl Sci Res* 37(1):65
26. Systèmes D (2014) Abaqus 6.14 analysis user's manual
27. Hou B, Zhao H, Pattofatto S, Liu J, Li Y (2012) Inertia effects on the progressive crushing of aluminium honeycombs under impact loading. *Int J Solids Struct* 49(19–20):2754
28. Lesuer DR, Kay G, LeBlanc M (2001) Modeling large-strain, high-rate deformation in metals. Tech. rep., Lawrence Livermore National Lab., CA (US)
29. Ghahremaninezhad A, Ravi-Chandar K (2012) Ductile failure behavior of polycrystalline Al 6061–T6. *International journal of fracture* 174(2):177
30. Reddy T, Narayanamurthy V, Rao Y (2019) Effect of damage modelling in numerical simulation of crash energy absorption behaviour of crush tubes and validation with experiments. *Int J Crashworth* 25(4):447–457
31. Zang M, Hu Y, Zhang J, Ye W, Zhao M (2020) Crashworthiness of CFRP/aluminum alloy hybrid tubes under quasi-static axial crushing. *J Mater Res Technol* 9(4):7740
32. Zarei H, Kroeger M (2010) Crashworthiness investigation and optimization of empty and foam filled composite crash box. In: *Woven Fabric Engineering*. pp 343–362
33. Yamazaki K, Han J (1998) Maximization of the crushing energy absorption of tubes. *Struct Optim* 16(1):37
34. Lee SH, Kim HY, Oh SI (2002) Cylindrical tube optimization using response surface method based on stochastic process. *J Mater Process Technol* 130:490
35. Lanzi L, Castelletti L, Anghileri M (2004) Multi-objective optimisation of composite absorber shape under crashworthiness requirements. *Compos Struct* 65(3–4):433
36. Zarei H, Kröger M (2006) Multiobjective crashworthiness optimization of circular aluminum tubes. *Thin Walled Struct* 44(3):301
37. Liu Y (2008) Design optimisation of tapered thin-walled square tubes. *Int J Crashworth* 13(5):543
38. Costas M, Díaz J, Romera L, Hernández S (2014) A multi-objective surrogate-based optimization of the crashworthiness of a hybrid impact absorber. *Int J Mech Sci* 88:46
39. Karagöz S, Yıldız AR (2017) A comparison of recent metaheuristic algorithms for crashworthiness optimisation of vehicle thin-walled tubes considering sheet metal forming effects. *Int J Veh Des* 73(1–3):179
40. Wang C, Li Y, Zhao W, Zou S, Zhou G, Wang Y (2018) Structure design and multi-objective optimization of a novel crash box based on biomimetic structure. *Int J Mech Sci* 138:489
41. Chen T, Zhang Y, Lin J, Lu Y (2019) Theoretical analysis and crashworthiness optimization of hybrid multi-cell structures. *Thin Walled Struct* 142:116
42. Pirmohammad S, Esmaeili-Marzdashti S (2019) Multi-objective crashworthiness optimization of square and octagonal bitubal structures including different hole shapes. *Thin Walled Struct* 139:126
43. Baykasoğlu A, Baykasoğlu C, Çetin E (2020) Multi-objective crashworthiness optimization of lattice structure filled thin-walled tubes. *Thin Walled Struct* 149:106630
44. Bahramian N, Khalkhali A (2020) Crashworthiness topology optimization of thin-walled square tubes, using modified bidirectional evolutionary structural optimization approach. *Thin Walled Struct* 147:106524

45. Goldberg DE (1989) Genetic algorithms in search, optimization and machine learning. Addison-Wesley Longman Publishing Co., Inc., Boston
46. Iman RL, Helton JC, Campbell JE (1981) An approach to sensitivity analysis of computer models: Part I-introduction, input variable selection and preliminary variable assessment. *J Qual Technol* 13(3):174
47. Tang B (1993) Orthogonal array-based Latin hypercubes. *J Am Stat Assoc* 88(424):1392
48. Myers RH, Montgomery DC, Anderson-Cook CM (2016) Response surface methodology: process and product optimization using designed experiments. Wiley, Hoboken
49. Acar E, Guler MA, Gerceker B, Cerit ME, Bayram B (2011) Multi-objective crashworthiness optimization of tapered thin-walled tubes with axisymmetric indentations. *Thin Walled Struct* 49(1):94
50. Jones DR, Schonlau M, Welch WJ (1998) Efficient global optimization of expensive black-box functions. *J Glob Optim* 13(4):455
51. Box GE, Draper NR (2007) Response surfaces, mixtures, and ridge analyses, vol 649. Wiley, Hoboken
52. Sacks J, Welch WJ, Mitchell TJ, Wynn HP (1989) Design and analysis of computer experiments. *Stat. Sci.* 4(4):409–423
53. Wansaseub K, Slesongsom S, Panagant N, Pholdee N, Bureerat S (2020) Surrogate-assisted reliability optimisation of an aircraft wing with static and dynamic aeroelastic constraints. *Int J Aeronaut Space Sci* 21:723–732
54. Buhmann MD (2003) Radial basis functions: theory and implementations, vol 12. Cambridge University Press, Cambridge
55. Pholdee N, Bureerat S (2012) Surrogate-assisted evolutionary optimizers for multiobjective design of a torque arm structure. *Appl Mech Mater Trans Tech Publ* 101:324–328
56. Bishop CM et al (1995) Neural networks for pattern recognition. Oxford University Press, Oxford
57. Cristianini N, Shawe-Taylor J et al (2000) An introduction to support vector machines and other kernel-based learning methods. Cambridge University Press, Cambridge

Publisher's Note Springer Nature remains neutral with regard to jurisdictional claims in published maps and institutional affiliations.